ISME - Incoherent Sampling of Multi-Echo data to minimize cardiac-induced noise in brain maps of R_2* and magnetic susceptibility

Quentin Raynaud[1*], Rita Oliveira[1*], Nadège Corbin[2], Yaël Balbastre[3], Ruud B. van Heeswijk[4], Antoine Lutti[1]

[1]*Laboratory for Research in Neuroimaging, Department for Clinical Neuroscience, Lausanne University Hospital and University of Lausanne, Lausanne, Switzerland*

[2]*Centre de Résonance Magnétique des Systèmes Biologiques, UMR5536, CNRS/University Bordeaux, Bordeaux, France*

[3]*Department of Experimental Psychology, University College London, London, United Kingdom*

[4]*Department of Diagnostic and Interventional Radiology, Lausanne University Hospital and University of Lausanne, Lausanne, Switzerland.*

*These authors contributed equally to this work.

Correspondence

Antoine Lutti

Laboratory for Research in Neuroimaging, Department for Clinical Neuroscience, Lausanne University Hospital, Ch. de Mont-Paisible 16, CH-1011 Lausanne

Email: antoine.lutti@chuv.ch

Abstract

Purpose

Brain maps of the MRI parameters R_2* and magnetic susceptibility (χ) enable the investigation of microscopic tissue changes associated with brain disease in patient populations. However, maps of R_2* and χ are computed from gradient-echo data acquired at multiple echo times and are affected by cardiac-induced physiological noise. In this study, we introduce ISME – a sampling strategy that minimizes the level of cardiac-induced noise in brain maps of R_2* and χ.

Methods

Cardiac-induced noise causes exponential-like effects on the decay of the signal magnitude that vary across the cardiac cycle, increasing the variability of R_2* and χ estimates. ISME uses phase-encoding gradients to shift the k-space frequency of the acquired data between consecutive readouts of a multi-echo train. As a result, the multi-echo data at a given k-space index is acquired at different phases of the cardiac cycle. We compare the variability of R_2* and χ maps acquired with ISME and with standard multi-echo trajectories in N=10 healthy volunteers. We also investigate the effect of both sampling strategies on the spatial aliasing of pulsating MR signals in R_2* and χ maps and propose a weighted-least square (NWLS) approach for the estimation of R_2* that accounts for the increase in cardiac-induced noise with echo time.

Results

Compared to standard multi-echo trajectories, ISME reduces the variability of R_2* and χ across repetitions by 25/26/21% and 24/32/23% in the cerebellum/brainstem/whole brain, respectively. With ISME, the spatial aliasing of pulsating MR signals is incoherent between raw echo images, leading to visually sharper R_2* maps. The proposed NWLS approach for the estimation of R_2* removes the dependence of the fitting residuals on echo time and brings an additional 3/2/1% reduction of the R_2* variability in the cerebellum/brainstem/whole brain.

Conclusion

ISME allows the mitigation of cardiac-induced noise in brain maps of R_2* and χ, improving reproducibility.

Keywords:

Brain; cardiac-induced noise; Physiological noise; quantitative MRI; R2*; QSM; MRI relaxometry;

1. Introduction

The transverse relaxation rate ($R_2^* = 1/T_2^*$)[1] and magnetic susceptibility (χ)[2] are markers of iron and myelin content within brain tissue[3,4] and allow the study of microscopic tissue change due to brain disease in patient populations.[5–7] Minimal noise levels in maps of R_2^* and χ are required to allow optimal sensitivity to brain change in neuroscience studies. However, because these maps are computed from gradient-recalled echo (GRE) data acquired with echo times of up to ~40ms,[7–9] they are particularly sensitive to noise that arises from physiological processes such as respiration and cardiac pulsation.[8,10]

Respiration-induced noise originates from periodic fluctuations of the magnetic field due to changes in air volume in the lungs.[11] The effects of respiration on brain MRI data are typically corrected using phase navigators that reduce the variability of R_2^* and χ maps by 23% and 12% across repetitions in white matter.[8] Cardiac-induced noise in MRI data is the result of multiple physiological mechanisms: cardiac pulsation generates a pressure wave that leads to head motion,[12] CSF pulsation[13,14] and deformation[15,16] of inferior regions such as the brainstem[17,18] and cerebellum.[19] Also, pulsatile vessel movement and periodic blood influx[20–24] lead to spatially-localized effects that are most pronounced in highly vascularized regions such as the orbitofrontal cortex[14,25] and periventricular regions.[25,26] Physiological effects that are coherent across a voxel, such as variation of the mean magnetic field across a voxel,[8,27] laminar flow,[28,29] and motion[30–32] result in a net phase shift of the signal and primarily affect magnetic susceptibility estimates. On the other hand, effects that are incoherent across a voxel (e.g. turbulent flow,[33] local B_0 inhomogeneities[34]) result in a net change of the magnitude of the signal and primarily affect R_2^* estimates. Cardiac pulsation has recently been reported to lead to variations of R_2^* by up to $3s^{-1}$ across the cardiac cycle and to account for ~35% of the variability of R_2^* maps across repetitions.[10]

The acquisition of R_2^* and χ data stretches over several minutes. Cardiac-induced noise in the acquired data cannot be regressed out retrospectively from the temporal evolution of the signal as is routinely done for functional MRI data.[35–37] Also, the effects of cardiac pulsation on the MR signal are spatially localized and are not compatible with the navigator techniques used for the correction of respiration- or motion-induced effects.[38,39] Instead, prospective strategies show promising potential to reduce the impact of cardiac-induced noise in the acquired data. Specially-designed k-space sampling trajectories lead to spatially-incoherent aliasing of cardiac-induced noise across the field of view of an individual image.[40,41] Setting the number of samples at each k-space index according to the local level of noise is effective to reduce cardiac-induced noise in R_2^*-mapping data.[42] However it does not consider the effect of cardiac-induced noise across the temporal dimension of the multi-echo data.

In this study, we introduce a new sampling strategy to reduce the level of cardiac-induced noise in multi-echo data used for the computation of R_2^* and χ maps. This sampling strategy is based on dispersing the effect of cardiac-induced noise along the temporal dimension of the multi-echo data: with ISME (Incoherent Sampling of Multi-Echo data), the k-space frequency of the acquired data is changed between consecutive readouts of the echo train. As a result, the multi-echo data at a given k-space index are acquired across different phases of the cardiac cycle. The goal of this study was to demonstrate that ISME leads to higher reproducibility of brain maps of R_2^* and χ than standard k-space sampling trajectories in healthy volunteers. We also investigated the effect of both sampling strategies on the spatial aliasing of cardiac pulsation effects in maps of R_2^* and χ and on the fitting residuals.

2. Methods

2.1. ISME

With standard multi-echo trajectories, data are acquired at a single k-space frequency after each radiofrequency (RF) excitation. To allow for full image encoding, this process is repeated across a suitable set of k-space frequencies. Because the repetition time is much smaller than the cardiac period (TR $\lesssim$ 50ms), the multi-echo data at each k-space frequency can be assumed to have been acquired at the same phase of the cardiac cycle (Figure 1A). Because cardiac pulsation leads to systematic changes of R_2* across the cardiac cycle,[10] this multi-echo data contains exponential-like effects of cardiac pulsation on signal decay, leading to a bias of the apparent R_2*. This bias depends on the phase of the cardiac cycle at the time of acquisition of the data (Figure 1B). To minimize the effect of cardiac pulsation on R_2* estimates, we introduce ISME (Incoherent Sampling of Multi-Echo data) - a new sampling strategy that allows to sample the cardiac phase incoherently along the echo dimension. With ISME, short gradient pulses are played out between each readout of the multi-echo train to shift the k-space index (Figure 1C). Upon completion of data acquisition, the data at each k-space index is made up of multiple echoes acquired at different phases of the cardiac cycle. With ISME, estimation of R_2* averages out the fluctuations of signal decay across the cardiac cycle, at the cost of larger fit residuals (Figure 1D).

In this conceptual description of ISME, the k-space index is a simple counter that reflects the sequential ordering of data sampling. It is independent of the physical coordinates of the k-space frequencies and of the k-space trajectory used for data acquisition (e.g. linear, spiral or radial). Also, the time span between consecutive indexes might be a single TR interval in the case of two data points acquired consecutively, or a longer time interval. Here, we consider the case of a 3D FLASH sequence with linear sampling, in which neighbouring points are acquired consecutively along the fast phase-encoding direction, for each phase-encoding step along the slow direction. With this trajectory, the time interval between consecutive data points along the fast phase-encoding direction is TR $\lesssim$ 50ms, much shorter than the typical cardiac period. Cardiac pulsation leads to a broad modulation of the MR signal across k-space along this phase-encoding direction. We therefore implemented ISME along the slow phase-encoding direction, for which the time interval between neighbouring points is $TR*N_{fast}$, where N_{fast} is the number of k-space indexes along the fast encoding direction.

With ISME, the multi-echo data at a single k-space index is acquired over a duration $TR*N_{fast}*N_{echo}$, where N_{echo} is the number of echoes. To fully populate the k-TE space of the data with the diagonal sampling pattern of ISME (top-left and bottom right corners of Figure 1C), the sampling trajectory of ISME is initiated beyond the k-space boundary determined from the image encoding parameters, at $k=-(N_{echo}-1)$ and $k=k_{end}-(N_{echo}-1)$. The RF receivers are blanked in this region of k-space (shaded areas of Figure 1C), resulting in an increase of scan time by $TR*N_{fast}*(N_{echo}-1)$.

2.2. MRI data acquisition

Eleven healthy volunteers (4 females, mean age=33±9 years old) were scanned on a 3T MRI system (Magnetom Prisma; Siemens Medical Systems, Erlangen, Germany) using a 64-channel head coil. Written informed consent was obtained from each participant prior to participation and the study was approved by the local ethics committee. The data from one participant was excluded from analysis due to strong motion artifacts (Supplementary material 1). Acquisition of the GRE data was conducted using a custom-made multi-echo 3D FLASH pulse sequence. The k-space trajectory was linear Cartesian. 14 echo images were acquired with a bipolar readout, with echo times TE=1.25ms to 16.85ms with 1.2ms echo spacing. The repetition time was TR=21ms, the RF excitation angle 12°, the voxel size was 1.2x1.2x1.2mm^3 and the field of view 208×192×144mm^3. The images were reconstructed on the MRI scanner with adaptive coil combination[43,44] and GRAPPA[45] with an

acceleration factor of 2. Phase navigators were used to correct for systematic phase differences between positive and negative readouts.[46] In pilot experiments, ISME was observed to mitigate aliasing artefacts of non-cardiac origin such as those due to eye movement (Supplementary material 2). To keep the focus of this study specifically on cardiac-induced effects, the imaging volume was tilted by 30 degrees in the sagittal plane to displace this artefact below the brain. The total scan time was 5:29 minutes for the standard multi-echo trajectory and 6:08 minutes (+12%) for ISME due to the k-space boundary excursions. Each sampling strategy was acquired 3 times, in a randomized order, to quantify the reproducibility of the data across repetitions.

One of the participants (male, 44 years old) underwent an additional MRI exam at a higher resolution (voxel size 0.8x0.8x0.8mm^3; TR/TE=35.55/2.3ms; 2.14ms echo spacing; 14 echoes; other parameters the same as above). During this exam, one multi-echo dataset with the standard multi-echo trajectory (18:52 minutes) and one with the proposed ISME (20:28 minutes, +8%) were acquired. This data is available online (10.5281/zenodo.13364051).

To allow accurate tissue segmentation and delineation of grey matter regions, a multi-parameter relaxometry protocol was also used for the acquisition of multi-echo 3D FLASH data with magnetization transfer (MT), proton density (PD) and T1-weighted contrast (RF excitation angle = 6°, 6° and 21° respectively; TR/TE=24.5/2.34ms; voxel size: 1.5x1.5x1.5mm^3; field of view: 176×240×256mm^3). 8 echo images were acquired for the T1- and PD-weighted contrasts and 6 for the MT-weighted contrast. B_1-field mapping data (voxel size: 4x4x4mm^3; TR/TE=200/39.1ms) and B_0-field mapping data (voxel size: 3x3x2.5mm^3; TR=700ms; TE_1/TE_2=4.92/7.38ms) were also acquired.[47,48]

2.3. Image segmentation

Maps of MTsat[49] were computed from the MT-, PD- and T1-weighted images using the hMRI toolbox (https://hMRI.info).[50] The MTsat maps and GRE data acquired with the standard multi-echo trajectory and ISME were co-registered using Statistical Parametric Mapping (SPM12, Wellcome Centre for Human Neuroimaging, London, UK).

Grey and white matter probabilities maps were obtained from the segmentation of the MTsat maps with SPM Unified Segmentation.[51–53] Whole-brain masks were defined from the voxels with a grey or white matter probability above 0.95. Because B_0-field inhomogeneities affect the transverse decay of the MR signal,[54] voxels in the proximity of the air/tissue interface (e.g. Orbitofrontal cortex, amygdala, temporal lobe, hippocampus) were removed from the masks. Brainstem and cerebellum regions of interest (ROIs), in close proximity to the ventricles, carotid arteries and large blood vessels were defined from the labelled data provided by Neuromorphometrics, Inc. (http://neuromorphometrics.com/) under academic subscription, and were set to contain voxels with a grey or white matter probability above 0.95.

2.4. Relaxometry

Data were analysed using bespoke analysis scripts written in MATLAB R2021a (The Mathworks, Natick, MA). Before the estimation of R_2*, the distribution of signal intensities in the background voxels of the magnitude images was fitted with a Rician distribution. The value of the noncentrality parameter was deducted from the signal intensities to suppress the noise floor in these images. The signal intensities in each voxel of the magnitude images were then fitted with the following model:

$$S(TE) = S_0 \exp(-R_2^* TE) + \varepsilon \quad [1]$$

where S_0 is the signal amplitude at $TE = 0$ and ε is the residual error. Fitting was conducted using the non-linear least square (NLS) *lsqnonlin* MATLAB function with a trust-region-reflective algorithm. R_2*

was bounded between 1 to $80s^{-1}$ and its initial value was $20s^{-1}$. The root-mean-squared error (RMSE) of the fit was computed as a measure of the goodness of fit.

The NLS approach for the estimation of R_2* assigns an equal contribution of all echo images to the error estimates, regardless of their respective echo times. Alternatively, we also computed maps of R_2* using a nonlinear weighted least squares (NWLS) approach, with weights that reflect the noise level in each individual echo image. Estimation of the image-specific weights was conducted on the model of the QUIQI technique, which addresses the effect of motion degradation on the noise level in image analyses.[55–57] The noise level in the multi-echo data was modelled as a polynomial function of the echo time. The polynomial coefficients were estimated using the implementation of the Restricted Maximum Likelihood (ReML) of SPM[58] (Supplementary material 3, Matlab code available online (10.5281/zenodo.14808609)). The optimal order of this polynomial, which maximized the estimates of the evidence lower bound (ELBO) provided by ReML, was 4. The image-specific weights were computed as the inverse of the noise covariance matrix estimated by REML with the optimal noise model. These weights were then used to estimate R_2* according to eq. [1], using the non-linear least square *lsqnonlin* MATLAB function.

2.5. Quantitative susceptibility mapping

Quantitative magnetic susceptibility maps were generated from the phase of the MR data using bespoke scripts adapted from https://github.com/fil-physics/MPM_QSM. We used ROMEO[59] for the unwrapping of the phase images and ASPIRE[46] to remove the systematic phase differences between odd and even echo images. After segmentation of the first echo magnitude image with SPM's Unified Segmentation,[53] brain masks were defined to include voxels with a combined grey matter, white matter and CSF probability above 0 and with values of the ROMEO[59] phase quality metric above 0.3. Any holes present within the resulting mask were subsequently filled using the MATLAB function *imfill*. The spurious contribution of the background field to the phase data was removed using the Projection onto Dipole Fields algorithm[60] available in the SEPIA toolbox.[61] Finally, dipole inversion was conducted using the STAR-QSM algorithm[62] available in the SEPIA toolbox, using the entire brain as a reference.

2.6. Statistical analyses

The effects of cardiac pulsation on the MR signal lead to changes of the apparent R_2* across the cardiac cycle.[10] With standard multi-echo trajectories, the multi-echo data at a given k-space frequency is acquired for a given phase of the cardiac cycle and cardiac-induced noise increases the variability of the data across repetitions.[10] With ISME, multi-echo data representative of the whole cardiac cycle are acquired for each repetition (Figure 1). We conducted statistical analyses to test if this leads to reduced data variability compared to standard multi-echo trajectories. We conducted paired Student's t-tests of the standard deviation (SD) of the R_2* and χ estimates across repetitions, for data acquired using the standard multi-echo trajectory and ISME.

With ISME, the effect of cardiac-induced noise on signal decay does not follow the exponential dependence on echo time of data acquired with standard multi-echo trajectories. We conducted statistical analyses to verify that this leads to higher levels of RMSE. We conducted paired Student's t-test analyses of the RMSE levels following estimation of R_2*, for data acquired using the standard multi-echo trajectory and ISME.

3. Results

In individual echo images acquired using both the standard multi-echo trajectory and ISME, the k-space data along the slow phase encoding direction are acquired at different phases of the cardiac cycle, leading to spatial aliasing of pulsating veins (Figure 2A and C). With the standard multi-echo trajectory, the distribution of the cardiac phase along the slow phase encoding direction is unchanged across echo

images (Figure 1A) and the resulting R_2* maps also display spatial aliasing (Figure 2B). With ISME, the distribution of the phase of the cardiac phase along the slow phase encoding direction differs between echo images (Figure 1C) and the R_2* maps computed from the signal decay across echoes show a reduced level of aliasing (Figure 2D).

The SD of R_2* across repetitions can reach up to $5s^{-1}$ in inferior brain regions in data acquired with the standard multi-echo trajectory (Figure 3A). The most affected areas include the cerebellum and brainstems – two of the regions most affected by cardiac-induced noise.[10] The SD of R_2* is much reduced in inferior brain regions with the ISME approach, leading to variability maps that are more spatially uniform. With ISME, the SD of R_2* across repetitions was reduced by 25, 26, and 21% in the cerebellum, brainstem and whole brain compared to the standard multi-echo trajectory, for a 12% increase in scan time (Table 1 and Figure 3, $p \leq 0.001$). Under the simplifying assumption of independent uncorrelated noise, a similar reduction with standard multi-echo trajectory would require an increase in scan time by a factor 1.25^2, i.e. 56%. Much of these observations are also applicable to maps of χ (Figure 4A). ISME reduces the SD of χ estimates across repetitions by 24, 32, and 23% in the cerebellum, brainstem, and whole brain, respectively, compared to the standard multi-echo trajectory (Table 1 and Figure 4, $p \leq 0.001$).

With the standard multi-echo trajectory, the maps of the goodness of fit of the multi-echo data with the exponential decay model (RMSE) show a sharp decrease from the brain periphery to central brain regions that mirrors the sensitivity profile of the receive coil (Figure 5A). Data acquired with the proposed ISME approach exhibit higher RMSE levels and a high level of spatial aliasing along the slow phase encoding direction. This increase is stronger in inferior brain areas and around the circle of Willis: the RMSE increases by 18, 13 and 15% in the cerebellum, brainstem and whole brain with the ISME approach (Table 1 and Figure 5B, $p \leq 0.001$).

The variance across repetitions of the residual error, a measure of the noise level in the data, increases with echo time for both acquisition strategies (Figure 5C). However, this increase is more pronounced with ISME: assuming a linear increase, the slope reaches 0.49, 0.38 and 0.22 [a.u./ms] in the cerebellum, brainstem and whole brain with ISME and 0.23, 0.17 and 0.06 [a.u./ms] with the standard multi-echo trajectory in these regions (Figure 5D).

Using a NWLS approach to estimate R_2*, with weights computed using the proposed ReML-based approach (Figure 6A), allows the recovery of a uniform distribution of the residuals across echo times in data acquired with ISME (Figure 6B). Assuming a linear increase of the noise level with echo time, the slope reduces to 0.05, 0.03 and 0.19 [a.u./ms] in the cerebellum, brainstem and whole brain (0.49, 0.38 and 0.22 [a.u./ms] with NLS, see above) (Figure 6C). The proposed NWLS approach further reduces the SD of R_2* by 3% in the cerebellum, 2% in the brainstem and 1% in the whole-brain compared to the standard NLS (Table 1, $p \leq 0.001$).

4. Discussion

Cardiac pulsation generates exponential-like effects on the transverse decay of multi-echo GRE data, leading to systematic changes of R_2* across the cardiac cycle[10]. With standard trajectories, the multi-echo data is acquired at the same phase of the cardiac cycle, for each k-space frequency, leading to a bias on the R_2* estimates. Because the effect of cardiac pulsation depends on the timing of data acquisition relative to the cardiac cycle, cardiac-induced noise increases the variability of brain maps of the transverse relaxation rate (R_2*) and quantitative susceptibility (QSM) across repetitions. In this work, we proposed a new sampling strategy termed Incoherent Sampling of Multi-Echo data (ISME),

based on shifting k-space location between each readout of the multi-echo train. With ISME, the multi-echo data of each k-space frequency is made up of points acquired at different phases of the cardiac cycle, mitigating the effects of cardiac pulsation across echoes.

With ISME, estimation of R_2* and χ effectively averages out the effect of cardiac pulsation and leads to improved repeatability of the data across repetitions: over the whole brain, ISME reduces the variability of R_2* across repetitions by 21% compared to standard multi-echo trajectories. Similarly, the variability of χ estimates is reduced by 23% with ISME. The reduction in variability were most pronounced in inferior brain regions such as the brainstem and cerebellum (25-26% for R_2* maps and 24-32% for χ maps). Maps of the SD of R_2* and χ estimates across repetitions are spatially more uniform with ISME. These improvements in the variability of R_2* and χ maps are similar to those from an alternative sampling strategy based on optimizing the number of samples at each k-space location based on the local level of cardiac-induced noise.[42] The scan time increase is also comparable between both methods (12% vs 14%). However for ISME, this scan time increase is due to the diagonal pattern used to traverse the k-TE space of the data, which imposes a k-space boundary beyond that determined from the image encoding parameters. The use of advanced trajectories such as Gilbert curves might alleviate any scan time increase.[40,41] Also, ISME acts on all k-space frequencies of the data and might better mitigate spatially localized effects of cardiac pulsation.

With both standard multi-echo trajectories and ISME, neighbouring k-space data are acquired at different phases of the cardiac cycle. Therefore, individual echo images display spatial aliasing of pulsating MR signal across the field of view of the image. However, for the standard multi-echo trajectory, this aliasing is unchanged between echo images and the R_2* maps computed from the multi-echo data also exhibit aliasing. With the proposed ISME approach, aliasing artifacts vary across individual echo images because the phase of the cardiac cycle between neighbouring k-space indexes varies between images. As a result, spatial aliasing of pulsating MRI signal arising from e.g. blood vessels is strongly reduced in R_2* maps.

With standard multi-echo trajectories, cardiac-induced noise induces exponential-like effects on the decay of the multi-echo data that depends on the phase of cardiac cycle at the time of acquisition of the data. ISME allows the incoherent sampling of cardiac-induced noise in the multi-echo data, leading to a 13-18% increase in RMSE compared to standard multi-echo trajectories. Note that the higher RMSE with ISME does not imply that the effective noise level is higher: with ISME, the RMSE measures also include cardiac-induced effects that only manifest in the variability of R_2* and χ maps with standard multi-echo trajectories. ISME also leads to a more pronounced increase of noise with increasing echo time. To address this, we introduced a novel nonlinear weighted least squares (NWLS) approach for the estimation of R_2*, in which the weights are computed from the noise level of individual echo images. This approach recovers a uniform distribution of noise across echoes and brings in an additional small reduction in variability of R_2* across repetitions (1-3%). This approach may bring more pronounced benefits with more complex models of transverse relaxation.[63,64] Combined, the proposed ISME approach and NWLS estimation might allow the data to better comply with the requirements of independent and identically distributed noise for the denoising of multi-echo data.[65,66] Here, analysis of the RMSE and estimation using the proposed weighted least square approach was not conducted for χ as we only had access to compiled code for the estimation for this MRI parameter.

This work was motivated by the known effects of cardiac-induced noise on brain maps of R_2*.[10] While the specific effects of cardiac-induced noise on magnetic susceptibility data are unknown, the existing literature points to breathing noise as the dominant source of noise.[8] Breathing induces periodic fluctuations of the main magnetic field B_0 in the head due to changes of the air volume in the lungs,[8,67] and to corresponding changes in the increase of the signal phase with echo time.[27,68] With ISME, multi-

echo data is acquired for different phases of the breathing cycle as well as cardiac cycle. We expect that effects of breathing on magnetic susceptibility estimates are also mitigated with ISME.

ISME shifts the current value of the k-space index between each readout of the multi-echo train. The k-space index is independent of the physical coordinates of the k-space data, and ISME is readily transferable to most sampling trajectories. Here we implemented ISME in a linear Cartesian scheme but it could equally be implemented in other trajectories. For example a pseudo-spiral trajectory has been used recently to reduce the level of cardiac-induced noise by increasing the number of samples near the k-space centre.[42] The combination of these two strategies could be beneficial e.g. when too few echo images are acquired to effectively sample the cardiac cycle between echoes with ISME alone. However, hardware limitations (amplitude, slew rate,…) might impose limits on the gradients required to shift the k-space index between the readouts. The impact of the eddy currents induced by these gradients on image quality should be carefully considered and might pose a practical limitation on the implementation of ISME in alternative sampling trajectories.

5. Conclusion

In this work, we proposed a new sampling strategy that reduce the effect of cardiac pulsation on estimates of the transverse relaxation rate (R_2*) and magnetic susceptibility (χ) computed from multi-echo gradient-echo data. The proposed sampling strategy, termed Incoherent Sampling of Multi-Echo data (ISME), is based on shifting the k-space position of the acquired data between each readout of the multi-echo train. With ISME, the multi-echo data is made up of points acquired at different phases of the cardiac cycle. As a result, the variability of R_2*/ χ maps across repetitions is reduced by 20-25% / 23-32% compared to standard multi-echo trajectories. With ISME, the spatial aliasing of pulsating MR signal is incoherent across the set of multi-echo images. This allows effective reduction of this aliasing in the R_2* maps computed from the data.

MRI data acquired with ISME show a stronger increase of the noise level with echo time. We introduce a novel nonlinear weighted-least squares (NWLS) approach for the computation of R_2* maps, in which the weights are computed from the noise covariance matrix of the data – estimated using Restricted Maximum Likelihood. The proposed NWLS approach ensures a uniform noise distribution across echo times.

ISME allows the effective reduction of cardiac-induced noise in in vivo gradient-echo data and enhances the sensitivity of R_2* and χ estimates to brain change in neuroscience studies.

Data availability statement

The high-resolution dataset is available online here (10.5281/zenodo.13364051). The Matlab code used for the estimation of the image-specific weights is available online here (10.5281/zenodo.14808609).

Funding information

This work was supported by the Swiss National Science Foundation (grant no 320030_184784 (AL); 32003B_182615 (RBvH) and CRSII5_202276 (RBvH)).

Ethics approval statement

This study received approval from the local Ethics Committee and all participants gave their written informed consent prior to participation.

6. Figures:

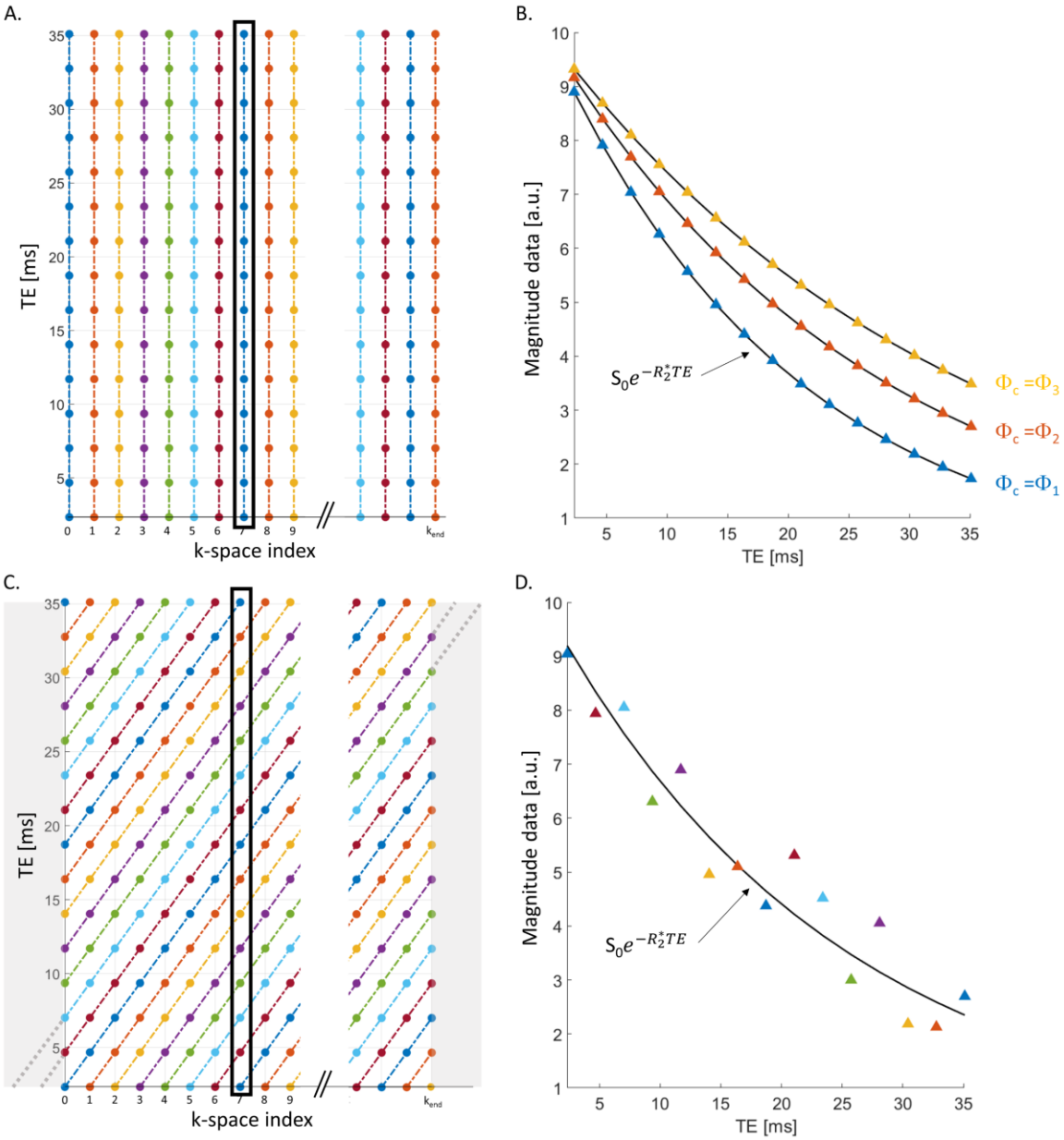

Figure 1: Traversal of the k-TE space with a standard multi-echo trajectory and with ISME. The different colours represent different phases of the cardiac cycle. With a standard multi-echo trajectory, multi-echo data is acquired at a distinct k-space frequency following each radio-frequency excitation (A). Because the repetition time is much smaller than the cardiac period (TR $\lesssim$ 50ms), the multi-echo data at each k-space frequency is effectively acquired at the same phase of the cardiac cycle. This multi-echo data contains exponential-like effects of cardiac pulsation on signal decay that depend on the phase of the cardiac cycle at the time of acquisition of the data (B). To minimize the effect of cardiac pulsation on R_2* estimates, the proposed ISME strategy shifts the current value of the k-space index between the readouts of the multi-echo train (C). As a result, the multi-echo data of each k-space location is made up of points acquired at different phases of the cardiac cycle (D).

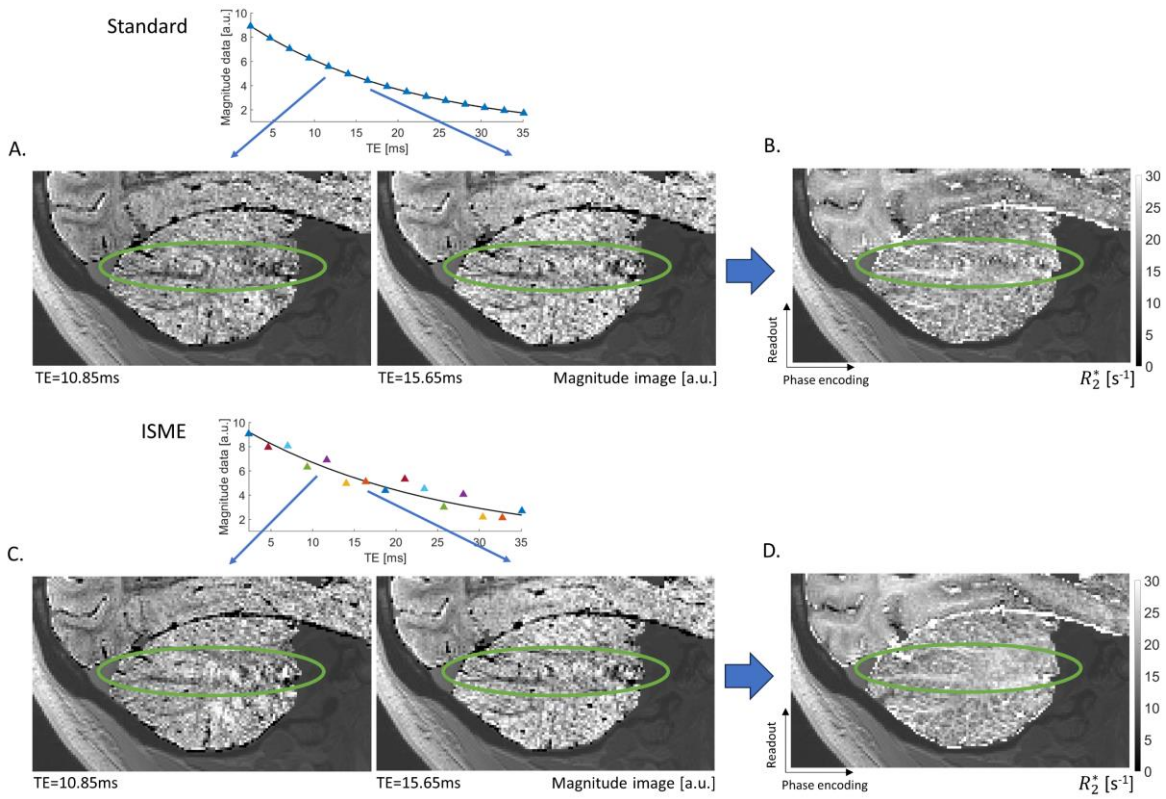

Figure 2: Example individual echo magnitude images, and corresponding R_2* map computed from the signal decay across echoes. Aliasing of pulsating signal originating from the nearby carotid artery can be seen on the individual echo images acquired with both the standard multi-echo trajectory (A) and ISME (C) (green circles). For the standard multi-echo trajectory, the spatial aliasing is consistent across all echoes and is clearly visible on the corresponding R_2* map (B). With the ISME approach, the spatial aliasing varies across echo images and is largely mitigated in the corresponding R_2* maps.

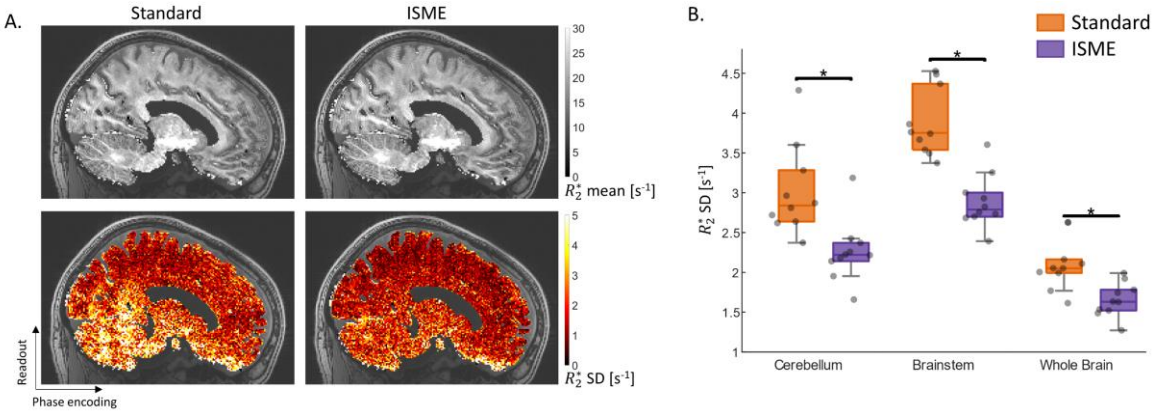

Figure 3: (A) Example mean and SD across repetitions of R_2* maps computed from data acquired with the standard multi-echo trajectory and ISME. (B) ROI-averaged SD of R_2* in the cerebellum, brainstem and whole brain for each subject. ISME reduces the SD of R_2* across repetitions by 25, 26 and 21% in the cerebellum, brainstem and whole brain, respectively ($p \leq 0.001$) compared to the standard multi-echo trajectory.

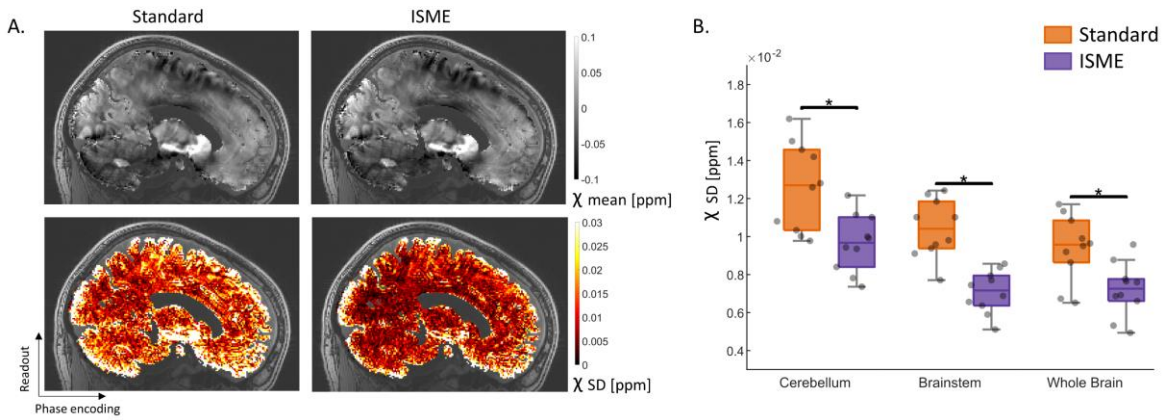

Figure 4: (A) Example mean and SD across repetitions of magnetic susceptibility (χ) maps computed from data acquired with the standard multi-echo trajectory and ISME. (B) ROI-averaged SD of χ estimates in the cerebellum, brainstem and whole brain for each subject. ISME reduces the SD of χ estimates across repetitions by 24, 32 and 23% in the cerebellum, brainstem and whole brain, respectively (p≤0.001) compared to the standard multi-echo trajectory.

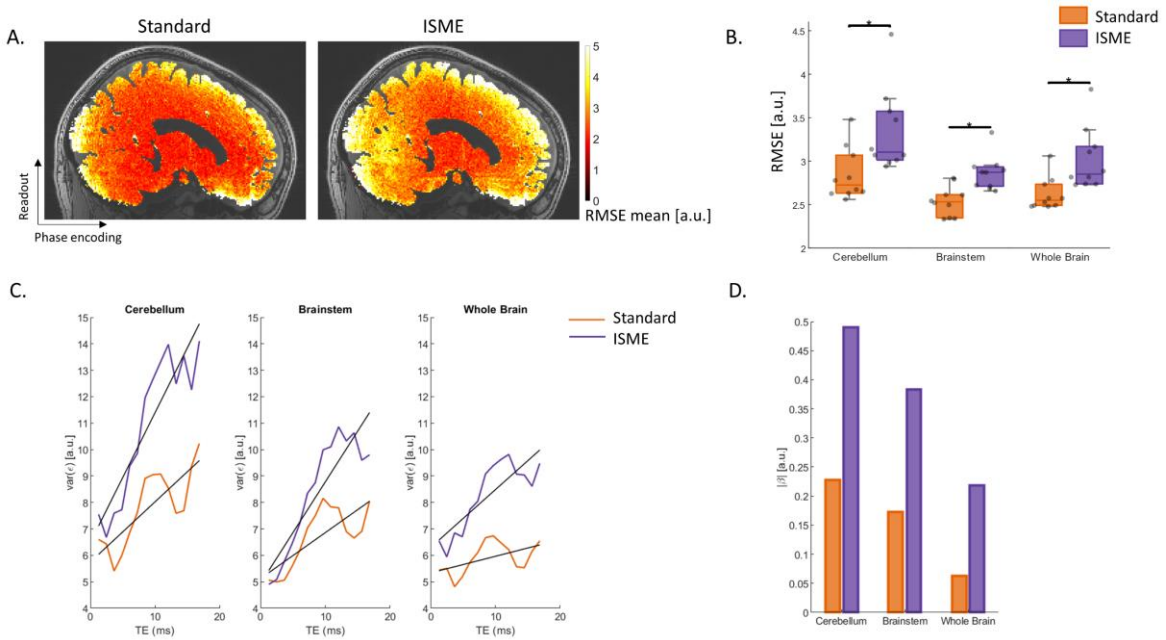

Figure 5: (A) Mean root mean square error (RMSE) map of R_2* fits across repetitions, computed from data acquired with a standard multi-echo trajectory and with ISME. (B) Regional RMSE levels in the cerebellum, brainstem and whole brain. RMSE is higher with ISME by 18, 13 and 15% (p≤0.001). (C) Variance of the residuals (ε) across repetitions as a function of echo time for both the standard multi-echo trajectory (orange) and ISME (purple), in the cerebellum, brainstem and whole brain. (D) Assuming a linear dependence, ISME data exhibits a stronger change of the residual variance with echo time ($|\beta| \approx$ 0.49, 0.38, 0.22 [a.u./ms]) than the standard multi-echo trajectory ($|\beta| \approx$ 0.23, 0.17, 0.06 [a.u./ms]) in the cerebellum, brainstem and whole-brain respectively.

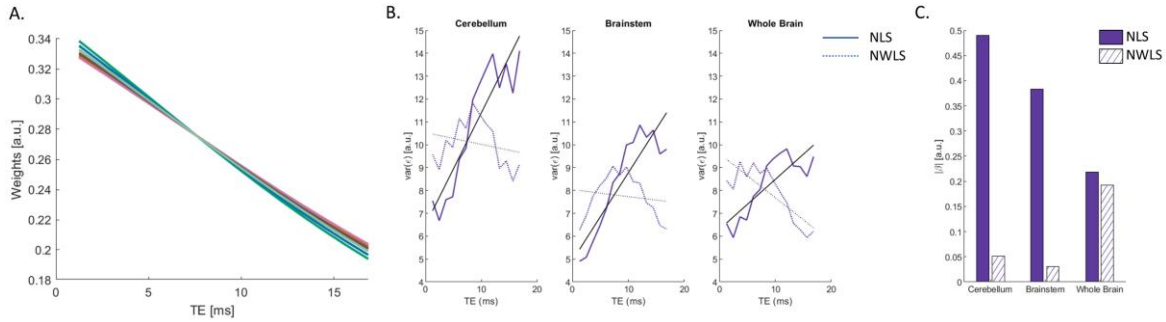

Figure 6: (A) Weights computed with the proposed NWLS approach for each study participant. The lower weights at long echo times are due to the higher noise level in the corresponding echo images. (B) Variance of the residuals (ε) across repetitions as a function of echo time, following estimation of R_2* from the ISME data with the NLS and NWLS approach. (C) The linear dependence of the residual variance with NLS fitting ($|\beta| \approx 0.49, 0.38, 0.22$ [a.u./ms] in the cerebellum, brainstem, whole-brain), is reduced with the NWLS fitting approach ($|\beta| \approx 0.05, 0.03, 0.19$ [a.u./ms] in these regions).

7. Tables

	Trajectory	Brainstem	Cerebellum	Whole brain
R_2* SD [s^{-1}]	Standard	3.02±0.57	3.88±0.43	2.00±0.31
	ISME NLS	2.26±0.39	2.89±0.34	1.57±0.20
	ISME NWLS	2.20±0.35	2.83±0.29	1.56±0.20
RMSE [a.u.]	Standard	2.85±0.30	2.54±0.17	2.62±0.20
	ISME NLS	3.34±0.48	2.86±0.20	3.02±0.36
	ISME NWLS	3.27±0.43	2.77±0.18	2.99±0.33
χ SD [ppb]	Standard	12.63±2.32	10.41±1.54	8.72±1.67
	ISME	9.66±1.52	7.09±1.12	6.57±1.31

Table 1: Variability of R_2* estimates across repetitions, goodness of fit of the R_2* estimates (RMSE) and variability of magnetic susceptibility (χ) estimates across repetitions, from data acquired with a standard multi-echo trajectories and with ISME. For the data acquired with ISME, the R_2* variability and RMSE estimates were computed using nonlinear least squares (NLS) and nonlinear weighted least squares (NWLS).

8. Reference

1. Cohen-Adad J. What can we learn from T2* maps of the cortex? *NeuroImage*. 2014;93:189-200. doi:10.1016/j.neuroimage.2013.01.023

2. Deistung A, Schweser F, Reichenbach JR. Overview of quantitative susceptibility mapping. *NMR in Biomedicine*. 2017;30(4). doi:10.1002/nbm.3569

3. Fukunaga M, Li TQ, Van Gelderen P, et al. Layer-specific variation of iron content in cerebral cortex as a source of MRI contrast. *Proceedings of the National Academy of Sciences of the United States of America*. 2010;107(8):3834-3839. doi:10.1073/pnas.0911177107

4. Stüber C, Morawski M, Schäfer A, et al. Myelin and iron concentration in the human brain: A quantitative study of MRI contrast. *NeuroImage*. 2014;93(P1):95-106. doi:10.1016/j.neuroimage.2014.02.026

5. Langkammer C, Ropele S, Pirpamer L, Fazekas F, Schmidt R. MRI for iron mapping in Alzheimer's disease. *Neurodegenerative Diseases*. 2014;13(2-3):189-191. doi:10.1159/000353756

6. Ulla M, Bonny JM, Ouchchane L, Rieu I, Claise B, Durif F. Is R2* a New MRI Biomarker for the Progression of Parkinson's Disease? A Longitudinal Follow-Up. *PLoS ONE*. 2013;8(3). doi:10.1371/journal.pone.0057904

7. Ghadery C, Pirpamer L, Hofer E, et al. R2* mapping for brain iron: Associations with cognition in normal aging. *Neurobiology of Aging*. 2015;36(2):925-932. doi:10.1016/j.neurobiolaging.2014.09.013

8. Choi JY, Lee J, Nam Y, Lee J, Oh SH. Improvement of reproducibility in quantitative susceptibility mapping (QSM) and transverse relaxation rates (R2*) after physiological noise correction. *Journal of Magnetic Resonance Imaging*. 2019;49(6):1769-1776. doi:10.1002/jmri.26522

9. Khalil M, Enzinger C, Langkammer C, et al. Quantitative assessment of brain iron by R2* relaxometry in patients with clinically isolated syndrome and relapsing-remitting multiple sclerosis. *Multiple Sclerosis*. 2009;15(9):1048-1054. doi:10.1177/1352458509106609

10. Raynaud Q, Di Domenicantonio G, Yerly J, Dardano T, van Heeswijk RB, Lutti A. A characterization of cardiac-induced noise in R2* maps of the brain. *Magnetic Resonance in Medicine*. 2024;91(1):237-251. doi:10.1002/mrm.29853

11. Windischberger C, Langenberger H, Sycha T, et al. On the origin of respiratory artifacts in BOLD-EPI of the human brain. *Magnetic Resonance Imaging*. 2002;20(8):575-582. doi:10.1016/S0730-725X(02)00563-5

12. Maclaren J, Armstrong BSR, Barrows RT, et al. Measurement and Correction of Microscopic Head Motion during Magnetic Resonance Imaging of the Brain. *PLoS ONE*. 2012;7(11). doi:10.1371/journal.pone.0048088

13. Chen L, Beckett A, Verma A, Feinberg DA. Dynamics of respiratory and cardiac CSF motion revealed with real-time simultaneous multi-slice EPI velocity phase contrast imaging. *NeuroImage*. 2015;122:281-287. doi:10.1016/j.neuroimage.2015.07.073

14. Hermes D, Wu H, Kerr AB, Wandell BA. Measuring brain beats: Cardiac-aligned fast functional magnetic resonance imaging signals. *Human Brain Mapping*. 2023;44(1):280-294. doi:10.1002/hbm.26128

15. Sloots JJ, Froeling M, Biessels GJ, Zwanenburg JJM. Dynamic brain ADC variations over the cardiac cycle and their relation to tissue strain assessed with DENSE at high-field MRI. *Magnetic Resonance in Medicine*. 2022;88(1):266-279. doi:10.1002/mrm.29209

16. Adams AL, Viergever MA, Luijten PR, Zwanenburg JJM. Validating faster DENSE measurements of cardiac-induced brain tissue expansion as a potential tool for investigating cerebral microvascular pulsations. *NeuroImage*. 2020;208. doi:10.1016/j.neuroimage.2019.116466

17. Brooks JCW, Faull OK, Pattinson KTS, Jenkinson M. Physiological noise in brainstem fMRI. *Frontiers in Human Neuroscience*. 2013;(OCT). doi:10.3389/fnhum.2013.00623

18. Beissner F. Functional MRI of the Brainstem: Common Problems and their Solutions. *Clinical Neuroradiology*. 2015;25:251-257. doi:10.1007/s00062-015-0404-0

19. van der Zwaag W, Jorge J, Butticaz D, Gruetter R. Physiological noise in human cerebellar fMRI. *Magnetic Resonance Materials in Physics, Biology and Medicine*. 2015;28(5):485-492. doi:10.1007/s10334-015-0483-6

20. Bianciardi M, Toschi N, Polimeni JR, et al. The pulsatility volume index: An indicator of cerebrovascular compliance based on fast magnetic resonance imaging of cardiac and respiratory pulsatility. *Philosophical Transactions of the Royal Society A: Mathematical, Physical and Engineering Sciences*. 2016;374(2067). doi:10.1098/rsta.2015.0184

21. Morgan AG, Thrippleton MJ, Wardlaw JM, Marshall I. 4D flow MRI for non-invasive measurement of blood flow in the brain: A systematic review. *Journal of Cerebral Blood Flow and Metabolism*. 2021;41(2):206-218. doi:10.1177/0271678X20952014

22. Schuchardt F, Schroeder L, Anastasopoulos C, et al. In vivo analysis of physiological 3D blood flow of cerebral veins. *European Radiology*. 2015;25(8):2371-2380. doi:10.1007/s00330-014-3587-x

23. Petridou N, Schäfer A, Gowland P, Bowtell R. Phase vs. magnitude information in functional magnetic resonance imaging time series: toward understanding the noise. *Magnetic Resonance Imaging*. 2009;27(8):1046-1057. doi:10.1016/j.mri.2009.02.006

24. Menon RS. Postacquisition suppression of large-vessel BOLD signals in high-resolution fMRI. *Magnetic Resonance in Medicine*. 2002;47(1):1-9. doi:10.1002/mrm.10041

25. Dagli MS, Ingeholm JE, Haxby JV. Localization of cardiac-induced signal change in fMRI. *NeuroImage*. 1999;9(4):407-415. doi:10.1006/nimg.1998.0424

26. Deckers RHR, van Gelderen P, Ries M, et al. An adaptive filter for suppression of cardiac and respiratory noise in MRI time series data. *NeuroImage*. 2006;33(4):1072-1081. doi:10.1016/j.neuroimage.2006.08.006

27. Gelderen P van, Zwart JA de, Starewicz P, Hinks RS, Duyn JH. Real-Time Shimming to Compensate for Respiration- Induced B0 Fluctuations. *Magnetic Resonance in Medicine*. Published online 2007.

28. Larson TC, Kelly WM, Ehman RL, Wehrli FW. Spatial misregistration of vascular flow during MR imaging of the CNS: Cause and clinical significance. *American Journal of Neuroradiology*. 1990;11(5):1041-1048.

29. Wymer DT, Patel KP, Burke WF, Bhatia VK. Phase-contrast MRI: Physics, techniques, and clinical applications. *Radiographics*. 2020;40(1):122-140. doi:10.1148/rg.2020190039

30. Godenschweger F, Kägebein U, Stucht D, et al. Motion correction in MRI of the brain. *Physics in Medicine and Biology*. 2016;61(5):R32-R56. doi:10.1088/0031-9155/61/5/R32

31. Welch EB, Felmlee JP, Ehman RL, Manduca A. Motion correction using the k-space phase difference of orthogonal acquisitions. *Magnetic Resonance in Medicine*. 2002;48(1):147-156. doi:10.1002/mrm.10179

32. Zaitsev M, Maclaren J, Herbst M. Motion artifacts in MRI: A complex problem with many partial solutions. *Journal of Magnetic Resonance Imaging*. 2015;42(4):887-901. doi:10.1002/jmri.24850

33. Borup DD, Elkins CJ, Eaton JK. Effects of motion on MRI signal decay from micron-scale particles. *Journal of Magnetic Resonance*. 2019;305:152-161. doi:10.1016/j.jmr.2019.06.014

34. Yang X, Sammet S, Schmalbrock P, Knopp MV. Postprocessing correction for distortions in T2 decay caused by quadratic cross-Slice B0 inhomogeneity. *Magnetic Resonance in Medicine*. 2010;63(5):1258-1268. doi:10.1002/mrm.22316

35. Agrawal U, Brown EN, Lewis LD. Model-based physiological noise removal in fast fMRI. *NeuroImage*. 2020;205. doi:10.1016/j.neuroimage.2019.116231

36. Tijssen RHN, Jenkinson M, Brooks JCW, Jezzard P, Miller KL. Optimizing RetroICor and RetroKCor corrections for multi-shot 3D FMRI acquisitions. *NeuroImage*. 2014;84:394-405. doi:10.1016/j.neuroimage.2013.08.062

37. Glover GH, Li TQ, Ress D. Image-based method for retrospective correction of physiological motion effects in fMRI: RETROICOR. *Magnetic Resonance in Medicine*. 2000;44(1):162-167. doi:10.1002/1522-2594(200007)44:1<162::AID-MRM23>3.0.CO;2-E

38. Wallace TE, Kober T, Stockmann JP, Polimeni JR, Warfield SK, Afacan O. Real-time shimming with FID navigators. *Magnetic Resonance in Medicine*. 2022;88(6):2548-2563. doi:10.1002/mrm.29421

39. Wallace TE, Polimeni JR, Stockmann JP, et al. Dynamic distortion correction for functional MRI using FID navigators. *Magnetic Resonance in Medicine*. 2021;85(3):1294-1307. doi:10.1002/mrm.28505

40. Seginer A, Schmidt R. Messing up to clean up: Semi-randomized frequency selective space-filling curves to suppress physiological signal fluctuations in MRI. *Magnetic Resonance in Medicine*. 2023;90(6):2275-2289. doi:10.1002/mrm.29790

41. Seginer A, Niry D, Furman-Haran E, Kolb H, Schmidt R. Reducing blood flow pulsation artifacts in 3D time-of-flight angiography by locally scrambling the order of the acquisition at 3 T and 7 T. *Magnetic Resonance in Medicine*. Published online 2024. doi:10.1002/mrm.30196

42. Raynaud Q, Dardano T, Oliveira R, et al. Data acquisition strategies to reduce cardiac-induced noise in brain maps of R 2 * and magnetic susceptibility. *bioRxiv*. Published online 2024. doi:10.1101/2024.08.20.608759

43. Benner T, Jellus V, Wang R, et al. *Adaptive Combination of Phased Array Signals for Diffusion Imaging*.; 2017. https://www.researchgate.net/publication/265808112

44. Walsh DO, Gmitro AF, Marcellin MW. Adaptive reconstruction of phased array MR imagery. *Magnetic Resonance in Medicine*. 2000;43(5):682-690. doi:10.1002/(SICI)1522-2594(200005)43:5<682::AID-MRM10>3.0.CO;2-G

45. Griswold MA, Jakob PM, Heidemann RM, et al. Generalized Autocalibrating Partially Parallel Acquisitions (GRAPPA). *Magnetic Resonance in Medicine*. 2002;47(6):1202-1210. doi:10.1002/mrm.10171

46. Eckstein K, Dymerska B, Bachrata B, et al. Computationally Efficient Combination of Multi-channel Phase Data From Multi-echo Acquisitions (ASPIRE). *Magnetic Resonance in Medicine*. 2018;79(6):2996-3006. doi:10.1002/mrm.26963

47. Lutti A, Hutton C, Finsterbusch J, Helms G, Weiskopf N. Optimization and validation of methods for mapping of the radiofrequency transmit field at 3T. *Magnetic Resonance in Medicine*. 2010;64(1):229-238. doi:10.1002/mrm.22421

48. Lutti A, Stadler J, Josephs O, et al. Robust and fast whole brain mapping of the RF transmit field B1 at 7T. *PLoS ONE*. 2012;7(3). doi:10.1371/journal.pone.0032379

49. Helms G, Dathe H, Kallenberg K, Dechent P. High-resolution maps of magnetization transfer with inherent correction for RF inhomogeneity and T1 relaxation obtained from 3D FLASH MRI. *Magnetic Resonance in Medicine*. 2008;60(6):1396-1407. doi:10.1002/mrm.21732

50. Tabelow K, Balteau E, Ashburner J, et al. hMRI – A toolbox for quantitative MRI in neuroscience and clinical research. *NeuroImage*. 2019;194:191-210. doi:10.1016/j.neuroimage.2019.01.029

51. Helms G, Draganski B, Frackowiak R, Ashburner J, Weiskopf N. Improved segmentation of deep brain grey matter structures using magnetization transfer (MT) parameter maps. *NeuroImage*. 2009;47(1):194-198. doi:10.1016/j.neuroimage.2009.03.053

52. Weiskopf N, Suckling J, Williams G, et al. Quantitative multi-parameter mapping of R1, PD*, MT, and R2* at 3T: A multi-center validation. *Frontiers in Neuroscience*. 2013;(7 JUN). doi:10.3389/fnins.2013.00095

53. Ashburner J, Friston KJ. Unified segmentation. *NeuroImage*. 2005;26(3):839-851. doi:10.1016/j.neuroimage.2005.02.018

54. Weiskopf N, Hutton C, Josephs O, Turner R, Deichmann R. Optimized EPI for fMRI studies of the orbitofrontal cortex: Compensation of susceptibility-induced gradients in the readout direction. *Magnetic Resonance Materials in Physics, Biology and Medicine*. 2007;20(1):39-49. doi:10.1007/s10334-006-0067-6

55. Lutti A, Corbin N, Ashburner J, et al. Restoring statistical validity in group analyses of motion-corrupted MRI data. *Human Brain Mapping*. 2022;43(6):1973-1983. doi:10.1002/hbm.25767

56. Corbin N, Oliveira R, Raynaud Q, et al. Statistical analyses of motion-corrupted MRI relaxometry data computed from multiple scans. *Journal of Neuroscience Methods*. 2023;398. doi:10.1016/j.jneumeth.2023.109950

57. Castella R, Arn L, Dupuis E, Callaghan MF, Draganski B, Lutti A. Controlling motion artefact levels in MR images by suspending data acquisition during periods of head motion. *Magnetic Resonance in Medicine*. 2018;80(6):2415-2426. doi:10.1002/mrm.27214

58. Friston KJ, Penny W, Phillips C, Kiebel S, Hinton G, Ashburner J. Classical and Bayesian inference in neuroimaging: Theory. *NeuroImage*. 2002;16(2):465-483. doi:10.1006/nimg.2002.1090

59. Dymerska B, Eckstein K, Bachrata B, et al. Phase unwrapping with a rapid opensource minimum spanning tree algorithm (ROMEO). *Magnetic Resonance in Medicine*. 2021;85(4):2294-2308. doi:10.1002/mrm.28563

60. Hu W, Liu H, Chen D, et al. Coil combination of multichannel single voxel magnetic resonance spectroscopy with repeatedly sampled in vivo data. *Molecules*. 2021;26(13). doi:10.3390/molecules26133896

61. Chan KS, Marques JP. SEPIA—Susceptibility mapping pipeline tool for phase images. *NeuroImage*. 2021;227. doi:10.1016/j.neuroimage.2020.117611

62. Wei H, Dibb R, Zhou Y, et al. Streaking artifact reduction for quantitative susceptibility mapping of sources with large dynamic range. *NMR in Biomedicine*. 2015;28(10):1294-1303. doi:10.1002/nbm.3383

63. Chan KS, Chamberland M, Marques JP. On the performance of multi-compartment relaxometry for myelin water imaging (MCR-MWI) – test-retest repeatability and inter-protocol reproducibility. *NeuroImage*. 2023;266. doi:10.1016/j.neuroimage.2022.119824

64. Oliveira R, Raynaud Q, Jelescu I, Kiselev VG, Kirilina E, Lutti A. In-vivo characterization of magnetic inclusions in the subcortex from non-exponential transverse relaxation decay. *bioRxiv*. Published online January 1, 2024:2023.09.15.557912. doi:10.1101/2023.09.15.557912

65. Does MD, Olesen JL, Harkins KD, et al. Evaluation of principal component analysis image denoising on multi-exponential MRI relaxometry. *Magnetic Resonance in Medicine*. 2019;81(6):3503-3514. doi:10.1002/mrm.27658

66. Bustin A, Lima da Cruz G, Jaubert O, Lopez K, Botnar RM, Prieto C. High-dimensionality undersampled patch-based reconstruction (HD-PROST) for accelerated multi-contrast MRI. *Magnetic Resonance in Medicine*. 2019;81(6):3705-3719. doi:10.1002/mrm.27694

67. Marques JP, Bowtell R. Application of a fourier-based method for rapid calculation of field inhomogeneity due to spatial variation of magnetic susceptibility. *Concepts in Magnetic Resonance Part B: Magnetic Resonance Engineering*. 2005;25(1):65-78. doi:10.1002/cmr.b.20034

68. Cheng H, Li Y. Respiratory noise correction using phase information. *Magnetic Resonance Imaging*. 2010;28(4):574-582. doi:10.1016/j.mri.2009.12.014

69. Budrys T, Veikutis V, Lukosevicius S, Gleizniene R, Monastyreckiene E, Kulakiene I. Artifacts in magnetic resonance imaging: How it can really affect diagnostic image quality and confuse clinical diagnosis? *Journal of Vibroengineering*. 2018;20(2):1202-1213. doi:10.21595/jve.2018.19756

70. Cavanaugh JE, Neath AA. The Akaike information criterion: Background, derivation, properties, application, interpretation, and refinements. *Wiley Interdisciplinary Reviews: Computational Statistics*. 2019;11(3). doi:10.1002/wics.1460

71. Chen WC, Foxley S, Miller KL. Detecting microstructural properties of white matter based on compartmentalization of magnetic susceptibility. *NeuroImage*. 2013;70:1-9. doi:10.1016/j.neuroimage.2012.12.032

1. Supplementary material

1.1. Motion degradation index

The index introduced in Castella et al. [55–57] was calculated from each multi-echo dataset to estimate the level of image degradation caused by head motion ('Motion Degradation Index', MDI). The distribution of MDI values peaked at MDI ~$3.5s^{-1}$, reflecting an overall high image quality (Figure S1). However, four datasets from the same subject exhibit MDI values above $4s^{-1}$, indicative of poor quality due to head motion. The data from this subject was removed from subsequent analyses.

1.2. Mitigation of coherent non-cardiac noise

Eye movement during the acquisition of MRI data leads to image aliasing along the slow phase-encoding direction of a 3D-encoded image. When the slow phase-encoding direction is oriented along the anterior-posterior direction of the patient, this aliasing propagates across the brain with a standard multi-echo trajectory (Figure S2A). However, this aliasing artifact is largely mitigated with the proposed ISME approach (Figure S2B). To keep the focus of this study specifically on cardiac-induced effects, the imaging box was tilted by 30 degrees in the sagittal plane to displace this artefact below the brain.[69]

1.3. Model optimization for estimation of R2* using NWLS

Fitting a nonlinear model with a weighted LS approach involves two sets of unknowns: the model parameters and the weights, with the latter corresponding to the inverse of the variance of the residuals at each echo time. Estimating both sets of parameters by maximum-likelihood results in biased estimates of (co)variance, which in turn bias the estimated model parameters. In contrast, restricted maximum-likelihood approaches (ReML) yield unbiased estimates of variance. ReML, however, does not lend itself easily to nonlinear models. We therefore devised a two-step procedure, whereby a linear ReML estimate of variance is performed first using a Taylor expansion of the transverse signal decay, and the resulting weights are then used in a nonlinear weighted least square (NWLS) fit. ReML estimation was performed using the function `spm_reml` in SPM (the analysis script is provided with this article). The covariance matrix of the residual noise was assumed diagonal, with weights modelled as a polynomial in TE. As is standard in SPM, we assumed that this covariance matrix is shared across all voxels within a brain volume.

We identified the optimal order of the Taylor expansion (M) from the Akaike information criterion corrected for small sample size (AICc). The AICc rewards the goodness of fit and penalizes the number of estimated parameters.[70] The minimal values of the AICc were found for Taylor expansion orders of 1 and 2 (Figure S3A). We opted for a Taylor expansion of order M=2 to accommodate local deviations from the linear approximation of the signal decay due to e.g. high decay rate in iron-rich regions (pallidum, red nuclei, substantia nigra,..) or deviations from the exponential behaviour in white matter and sub-cortical areas.[63,64,71]

From the results of the NLS analyses shown in Figure 5C, models of the dependence of image noise (approximated by the standard deviation of the residuals across voxels) on the echo time of the data were assumed to follow a polynomial form of order N. Model selection was conducted from the estimates of the evidence lower bound (ELBO) provided by the implementation of ReML of the SPM software.[58] The ELBO favours the reduction of residual errors and penalises model complexity. An optimal noise model maximises the ELBO. Compared to N=0 (uniform noise level across echo times), the optimal noise model was found to be N=3 for data acquired with the standard multi-echo

trajectory. The corresponding increase in ELBO was $\Delta ELBO=ELBO_{N=3}-ELBO_{N=0}=43.3$ (Figure S3B). With the proposed ISME method, the optimal polynomial order was N=4. The corresponding increase in ELBO ($\Delta ELBO=ELBO_{N=4}-ELBO_{N=0}=73.1$) is higher than in data acquired with the standard multi-echo trajectory. Image-specific weights were computed as the inverse of the diagonal elements of the noise covariance matrix estimated by ReML. The dependence of the weights on the echo time of the data shows little change for values of N≥4 (Figure S3C).

2. Supplementary figures

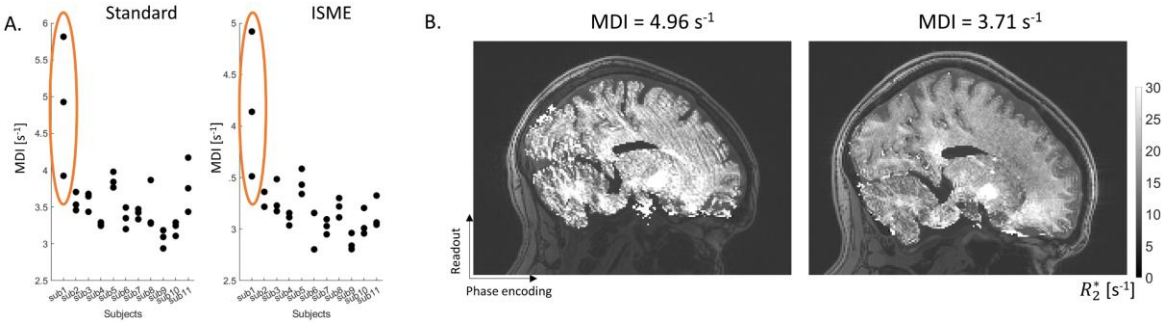

Figure S1: (A) Motion degradation index (MDI) of the datasets acquired with the standard multi-echo trajectory and ISME. The average MDI from subject 1 was 4.5±0.8s^{-1} and the average MDI amongst the other subjects was 3.3±0.3s^{-1}. (B) R_2* map computed from the first repetition of the standard multi-echo trajectory for subject 1 (MDI=4.96s^{-1}) and for one participant with MDI=3.71s^{-1}.

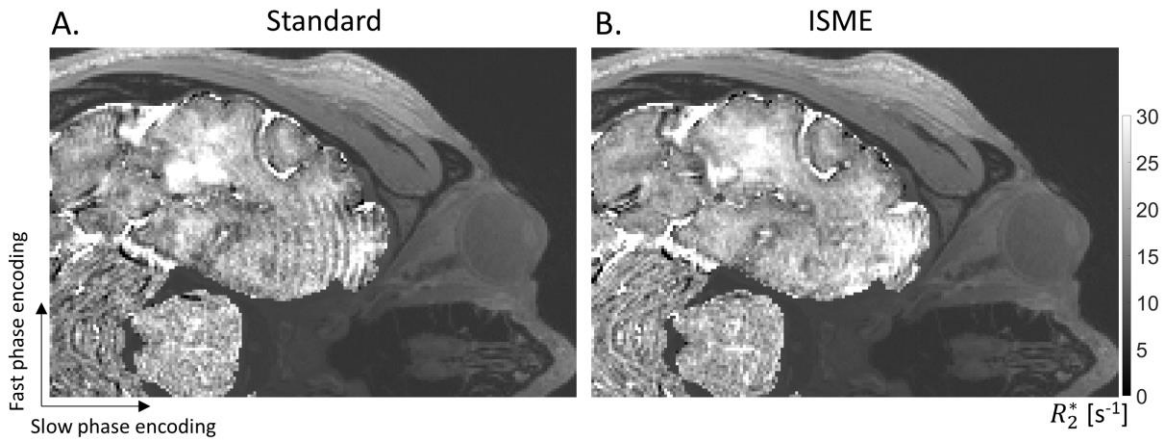

Figure S2: Eye movement during the acquisition of MRI data leads to image aliasing along the slow phase-encoding direction of a 3D-encoded image (blue arrows). This aliasing is present in data acquired with a standard multi-echo trajectory (A) but not with ISME (B).

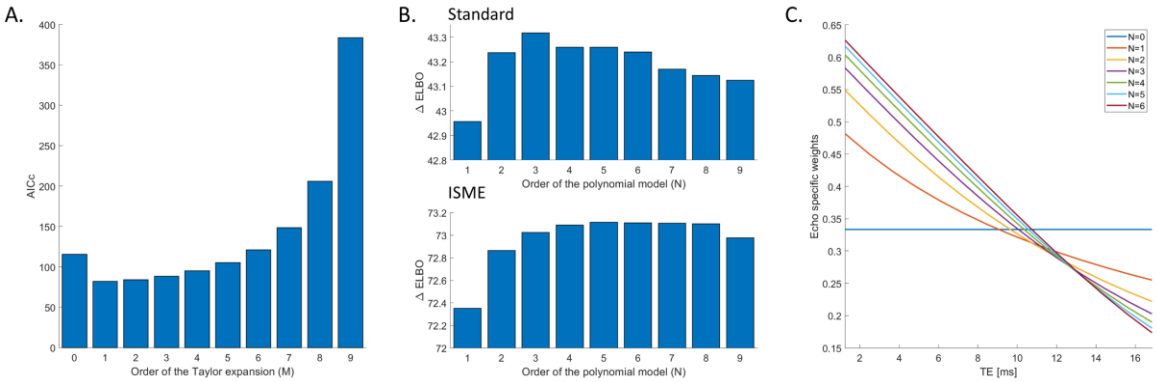

Figure S3: (A) Change in the Akaike information criterion (AICc) with the order of the Taylor expansion of the signal decay (M). (B) Increase of the evidence lower bound (ELBO) with the order of the polynomial model of the dependence of image noise on the echo time of the data (N), compared to N=0 (uniform noise level across echo times), for standard multi-echo trajectory and ISME. (C) Echo specific weights computed for different polynomial orders (M=2).